Communications in Physics, Vol. 34, No. 1 (2024), pp. 83-97
DOI: https://doi.org/10.15625/0868-3166/19184

Surface ferromagnetism of lead-free ferroelectric bismuth sodium titanate materials

Dang Duc Dung[1,†], **Vu Tien Lam**[1], **Nguyen Huu Lam**[1], **Duong Quoc Van**[2,‡], **Nguyen Hoang Thoan**[1], **Nguyen Hoang Linh**[1] **and Nguyen Ngoc Trung**[1]

[1]*Multifunctional Ferroics Materials Lab., Faculty of Engineering Physics, Hanoi University of Science and Technology, 1 Dai Co Viet road, Hanoi, Vietnam*

[2]*Faculty of Physics, Hanoi National University of Education, 136 Xuan Thuy street, Hanoi, Vietnam*

E-mail: [†]dung.dangduc@hust.edu.vn; [‡]vandq@hnue.edu.vn

Received 15 April 2023; *Accepted for publication 18 December 2023*; *Published 5 February 2024*

Abstract. *The role of complex surface defect on the magnet at the (110) surface of bismuth sodium titanate* ($Bi_{0.5}Na_{0.5}TiO_3$) *was discussed based on the first-principles calculation. The first-principle calculations for various types of surface defects exhibited the existence of magnetic moments for selected chemical and position defects. Specifically,* Na *and* Bi *vacancies induced large magnetic moments of* $0.52\mu_B$*/ f.u and* $0.50\mu_B$/f.*u, respectively, which were larger than that of Ti vacancies of* $0.01\mu_B$*/ f.u. Interestingly, oxygen vacancies did not induce local magnetic moments. Furthermore, significant magnetic moments of* $0.50\mu_B$*/ f.u and* $0.49\mu_B$*/ f.u were obtained for* Na *and Bi interstitial defects, while the local magnetic moments were slightly achieved around* $0.03\mu_B$*/ f.u and* $0.04\mu_B$*/ f.u for* Ti *and* O *interstitial defects, respectively. Anti-site defects between* Bi *and* Na *at A-site in perovskite* ABO_3 *structure exhibited magnetic moments of* $0.55\mu_B$*/ f.u for* Na *anti-site at Bi-site and* $0.39\mu_B$*/ f.u for Bi anti-site at Na-site. Interestingly, anti-site defects between the A-site and B-site in perovskite* ABO_3 *structure resulted in larger magnetic moments, with values of* $0.57\mu_B$/f.*u and* $0.53\mu_B$*/ f.u obtained for Ti anti-site defects at the Bi-site and Na-site, respectively. Additionally, magnetic moments of 0.50* μ_B*/ f.u and* $0.54\mu_B$*/ f.u were achieved for* Bi *and* Na *anti-site defects at the Ti-site, respectively. We expected that our work further contributed to the understanding of the role of surface defects in the magnetism of* $Bi_{0.5}Na_{0.5}TiO_3$ *materials in integrating ferromagnetic properties into lead-free ferroelectric materials for smart electronic device applications.*

Keywords: $Bi_{0.5}Na_{0.5}TiO_3$; surface defects; multiferroic; magnetism; lead-free ferroelectric.

Classification numbers: 31.15.E-; 73.20.-r; 61.72.-y; 77.84.-s; 75.50.Dd.

1. Introduction

Lead-free ferroelectric $Bi_{0.5}Na_{0.5}TiO_3$ (BNT) materials have recently gained rapid attention in research due to their exceptional ferroelectricity and piezoelectricity, which are comparable to those of the currently used in $Pb(Zr,Ti)O_3$ materials [1]. Therefore, BNT materials hold great promise for replacing $Pb(Zr,Ti)O_3$ materials in electronic devices, as the latter often contains toxic Pb elements, comprising approximately 60wt% of its chemical composition [1, 2]. BNT materials are appealing due to their non-toxicity, large remnant polarization $\left(P_r \sim 38\mu C/cm^2\right)$, and high Curie temperature $(T_C \sim 320^\circ C)$ [1, 2]. Nonetheless, their high coercive field $(E_C \sim 73$ kV/cm) and high conductivity have posed challenges during the polarizing process, limiting their practical applications [1]. Recently, there has been growing interest in the development of multiferroic materials, which combine both ferroelectric and ferromagnetic properties. These materials have the potential to revolutionize the next generation of electronic devices [3,4]. Multiferroic materials exhibit unique properties where magnetic moments were possibly controlled by an applied external electrical field, while polarization was tuned by an applied external magnetic field [3, 4]. However, N. A. Hill *et al.* predicted that multiferroic materials were rare existed in nature because the mechanism of ferromagnetic ordering required filling a part of d electrons in the orbital of the transition metal, whereas ferroelectricity was typically associated with empty states in the d-orbital [5]. Combining symmetry arguments with firstprinciples calculations, Benedek et al. predicted that the interaction between ferroelectricity and octahedral rotations in a group of ABO_3 perovskite oxides plays an important role in suppressing ferroelectricity in ABO_3 materials, shedding light on the coordination preferences of A-site cations [6]. A recent review by Lone *et al.* summarized the current developments in multiferroic materials and highlighted their potential applications in microelectronic devices, sensors, storage devices (e.g. hard disk platters and magnetic read heads), as well as magnetoelectric sensors, magnetometers, antennas, and even extensions to magnetic anomaly detection, navigation, and biomagnetic sensing [7]. Therefore, significant research efforts have been focused on the development of multiferroic materials with a profound impact on various aspects of life, from academia to a joint industry and the start-up of new businesses [7].

Recent advancements have led to the discovery of room temperature ferromagnetism in pristine BNT materials, opening up new possibilities for their application in the next general electronic devices where their magnetism properties can be harnessed in addition to their ferroelectric properties [8–12]. Thanh et al. reported weak-ferromagnetic properties at room temperature in BNT materials and suggested that these properties could be enhanced by controlling the amounts of oxygen vacancies [8]. Dung *et al.* proposed that ferromagnetism in BNT compounds could be linked to Ti^{3+} and Na^{+}vacancies based on their observation of various defect chemistries using X-ray photoelectron spectroscopy [9]. Ruth et al. obtained room temperature multiferroicity and a magnetoelectric coupling coefficient of about $4.18 mV/Oe$ in Na-deficient BNT compounds through spin polarization of holes in the valence band [10]. Pattanayak et al. reported that the spin-polarized tunneling of electrons at interfaces interface between the grain of BNT compounds was also important for inducing magnetoresistance and magnetocapacitance [11]. Additionally, Ju et al. conducted experiments that demonstrated that room temperature ferromagnetism in BNT materials weakened after subsequent annealing in a vacuum at 900°C for 20 min, while it was significantly enhanced following subsequent annealing in an oxygen atmosphere at 900°C for

20 min [12]. These results were well explained by density function theory calculations with the local density approximation, which suggested that the observation of room temperature ferromagnetism in pristine BNT compounds could be originated from Na^{+}vacancies at/near the surface of BNT(100) nanograins, resulting in a magnetic moment of $0.85\mu_B$ due to the spin polarization of $O-2p$ and Ti-3d electrons [12]. Ju et al. also predicted that the observation of room temperature ferromagnetism in surface defects of BNT(100) materials was possibly enhanced by the absorption of oxygen at the defects in the surface [13]. Zhang et al. performed ab initio calculation for defect chemistry in BNT compounds with rhombohedral perovskite structure, indicating that Na^{+}or Ti^{4+} vacancies could induce magnetism, as opposed to Bi^{3+} or O^{2-} vacancies. The magnetism of Na^{+}or Ti^{4+} vacancies mainly originated from the polarization of $O-2p$ electrons [14]. Recently, Lam *et al.* predicted that the defects chemistry at surface BNT(110) were complexly induced the magnetic moments by using the first-principle calculations for electronic structure with a conventional cell containing 30 atoms, including $3Na, 3Bi, 6Ti$ and 18O atoms [15]. However, their work still encountered challenges in that *i*) the vacancies and anti-site defects were relatively high, around 33.3% at *A*-site (Na, and Bi-site) and 16.7% at *B*-site (Ti-site), and *ii*) the presence of anti-site between *A*-site and *B*-site remained unclear. Moreover, while the defect-induced magnetism in surface BNT materials was well consistent for the (100) direction in first-principle calculations, the domination direction was observed in experimental to be the (110) direction [9-13]. Interestingly, the defect at surface of BNT(110) direction was found to be favorable for crystal growth in experimental findings from X-ray diffraction as well as X-ray photoelectron spectroscopy [9]. Hence, we propose that the room-temperature ferromagnetism observed in BNT materials might be attributed to defects on the BNT(110) surface rather than the BNT(100) surface defects. Therefore, reducing the amounts of self-defects in BNT(110) surface in theoretical calculations in unicell to bring them in closer agreement with experimental data (less than 10%) was necessary [10].

In this work, we investigate the intricate and complex self-defect chemistry at the surface of BNT(110) with 60 atoms in the unit cell using the density-functional theory. Although the pristine BNT(110) surface is non-magnetic, we observed significant magnetic moments of 0.52 $\mu_B/$ f.u and $0.50\mu_B/$ f.u for Na and Bi vacancies, respectively, while Ti vacancies exhibited a magnetic moment of $0.01\mu_B/$ f.u. Interestingly, oxygen vacancies did not induce local magnetic moments. Na and Bi interstitial defects induced magnetic moments of $0.50\mu_B$/f.u and 0.49 $\mu_B/$ f.u, respectively, whereas Ti and O interstitial defects exhibited magnetic moments of 0.03 $\mu_B/$ f.u and $0.04\mu_B/$ f.u, respectively. Na(Bi) and Bi(Na) anti-site defects have magnetic moments of $0.55\mu_B/$ f.u and $0.39\mu_B/$ f.u for Na anti-site at Bi-site and Bi anti-site at Na-site, respectively, while magnetic moments of $0.57\mu_B$/f.u and $0.53\mu_B$/f.u were obtained for Ti antisite defects at Bi-site and Na-site, respectively.

2. Computational details

We performed first-principles calculations utilizing the density functional theory (DFT) with ultrasoft pseudopotentials within the framework of the Cambridge Serial Total Energy Package (CASTEP) module program [15, 16]. Our choice of exchange energy employed the generalized gradient approximation (GGA), the Perdew, Burke, and Ernzerhof (PBE) functional used to describe the electron exchange-correlation potential [15, 17]. The plane-wave basis functions cutoff energy was set at 500eV, which yields the convergence of the total energy to 1.0×10^{-6} $eV/atom$ and a Hellman-Feynman force below $0.01eV/\text{Å}$. A regular Monkhorst-Pack scheme

grid of $1 \times 2 \times 2k$-point was adopted to sample the Brillouin zone, determining the number of integration points used for the wave function in reciprocal space [15, 18].

Regarding the crystal structure of BNT materials, we employed a rhombohedral configuration with the $R3c$ space group, characterized by lattice constants $a = b = 5.488$Å$, c = 13.504$Å, and $\alpha = \beta = 90^\circ, \gamma = 120^\circ$ [15,19]. Atomic positions in BNT compounds adhered to experimental observations reported by Jones and Thomas [20]. Thus, the unit cell for BNT compounds was constructed with 60 atoms, which was double higher than that previously reported for calculations of the unit cell for $Bi_{0.5}Na_{0.5}TiO_3$ compounds [15]. To model the BNT(110) surface, we initiated by cleaving the geometry-optimized primitive cell of rhombohedral BNT compounds. Subsequently, we added a vacuum layer with a thickness of 20Å to create a supercell with dimensions of $3 \times 2 \times 1$ unit cells. In addition, it is worth noting that the GGA method often underestimates the bandgap, which can precisely compensate for the neglected spin-orbital coupling (SOC) effect [15, 21, 22]. Therefore, for this calculation, we consider that the GGA method can accurately estimate the bandgap of the BNT(110) surface, and as a result, the SOC is not included in this study.

3. Results and discussion

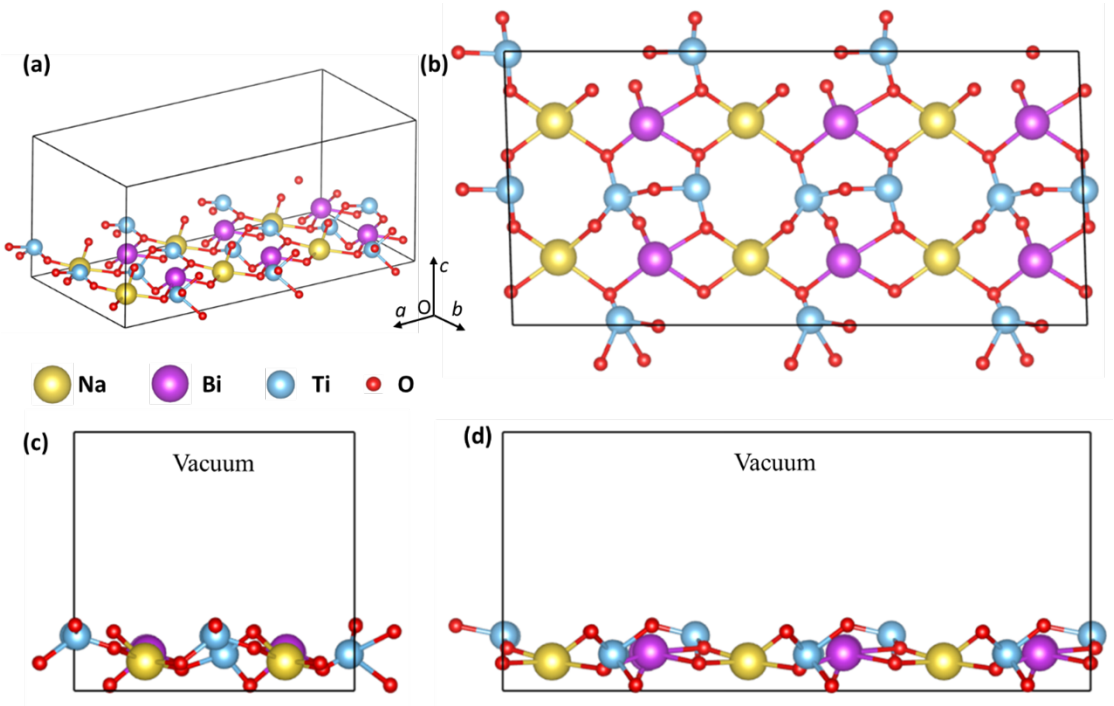

Fig. 1. The optimized structure of a perfect BNT(110) surface: (a) 3D view, (b) top view (Oc direction), (c) left-side view (Oa direction), and (d) right-site view (Ob direction).

Figure 1(a) illustrates the 3D view of the optimized perfect structure of the BNT(110) surface, with a chemical composition of 60 atoms represented as $Bi_6Na_6Ti_{12}O_{36}$. The structure consists of 6Bi atoms (in purple), 6Na atoms (in yellow), 12Ti atoms (in turquoise), and 36O atoms

(in red). In addition, the top view (in Oc direction), left-site view (O a direction), and right-site view (Ob direction) of the surface are also shown in Figs. 1 (b)-(d), respectively. The space group assigned to these surface configurations is $P1$ symmetry with the optimal lattice constants approximately of $a = 23.583$Å$, b = 11.242$Å$, c = 10.350$Å$, \alpha = \beta = 90^\circ$, and $\gamma = 91.81^\circ$ for the perfect BNT(110) surface. These results are consistent with recent reports on the surface calculation of BNT materials [15]. We proceeded to perform various defect chemistry calculations based on the initial BNT(110) surface, including vacancies, interstitials, and antisite defects.

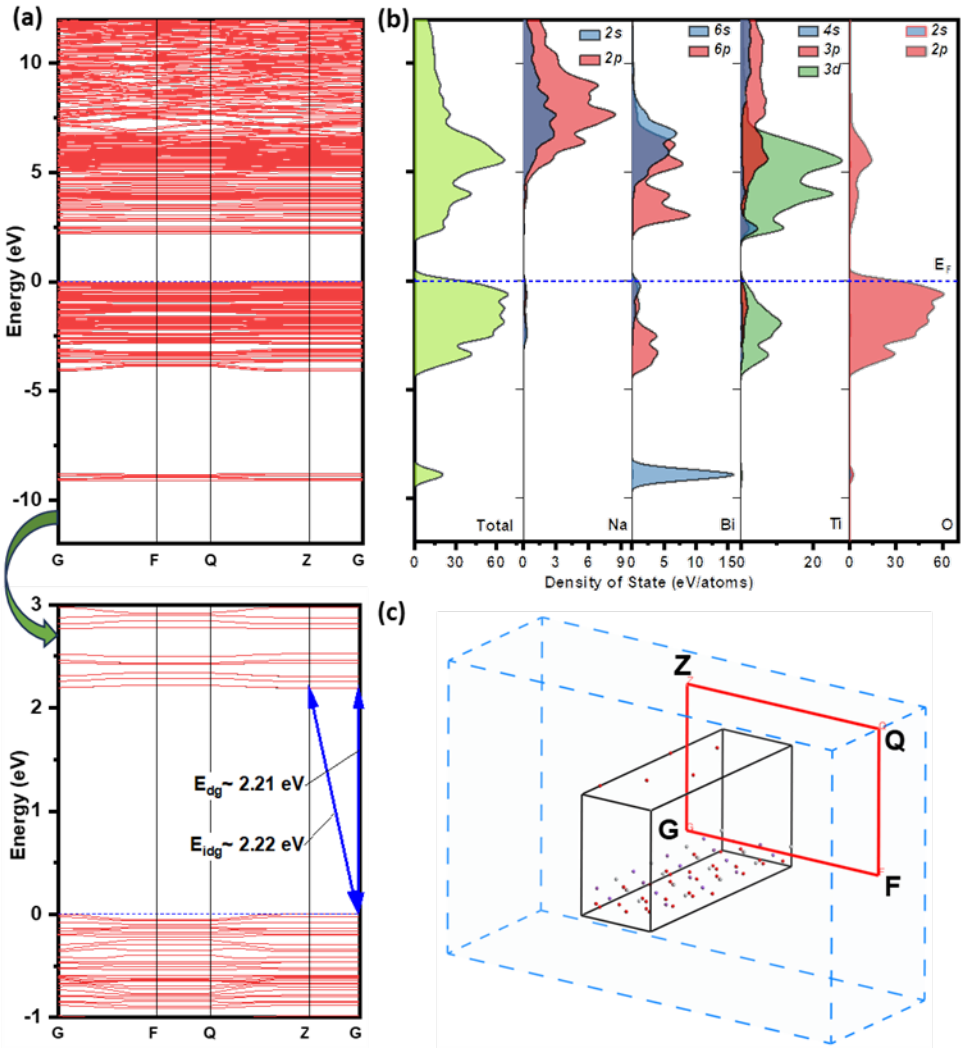

Fig. 2. (a) Electronic band structure, (b) partial density of states (PDOS) and total density of state (TDOS), and (c) Brillouin zone with positions of high-symmetry points of the perfect BNT(110) surface. High magnification of the electronic band structure of the BNT(110) surface is shown in the lower panel of Fig. 2(a).

The electronic band structure, the corresponding total density of state (TDOS), and the Brillouin zone with positions of high-symmetry points of the initial BNT(110) surface were shown in Figs. 2(a)-(c), respectively. In the electronic band structure, a bandgap was observed between the conduction band (CB) and valence band (VB), with the Fermi level (E_F) indicated by the blue dashed line. The results suggest that the BNT(110) surface exhibited characteristics of a semiconductor or insulator. This observation aligns well with experimental findings that classify BNT materials as ferroelectric insulators [1, 2]. However, distinguishing electron transition between CB and VB was challenging due to the closely spaced transition levels, as shown in the inset of Fig. 2(a). The direct transition electron from the G to G point between the CB and VB was estimated to be around $E_{dg} \sim 2.21$eV, while the indirect transition from G to Z point between the CB and VB was approximately $E_{idg} \sim 2.22$eV. Thus, the difference between E_{dg} and E_{idg} values was approximately 0.01eV, indicating the proximity of direct and indirect electron transitions between the CB and VB. These results were well consistent with recent electronic structural calculations of BNT(110) surface, which also found closely spaced direct and indirect transitions [15]. Recently, Behara et al. predicted that BNT exhibits both direct $\left(E_{dg} \sim 2.869\text{eV}\right)$ and indirect bandgap $\left(E_{idg} \sim 2.832\text{eV}\right)$, with a difference of approximately 0.037eV between the two gap energies [23]. Our calculations have well explained the experimental observations that suggest two distinct gap energies for BNT, approximately 3.05eV for direct and 2.86eV for indirect transitions [24]. Furthermore, Fig. 2(b) provided a clear representation of the electronic band structure of the BNT(110) surface, detailing the contribution of each element through the partial density of state (PDOS) and TDOS. The lowest valence band was situated around -9eV and was primarily composed of PDOS from Bi- 6s orbitals, with a minor contribution from $O-2p$ orbitals, known for inducing a significant ferroelectric polarization due to their lone pairs. The higher valence band was predominantly formed by PDOS from Bi- 6p and Ti-3d orbitals. Additionally, there is a minor contribution from PDOS of Bi- 6s orbitals and Ti-3p orbitals, which were closer to the E_F. The conduction band of the BNT(110) surface mainly consisted of PDOS from Ti-3d, Ti-4s, and Bi-6p orbitals. PDOS from $Na-2s$ and $Na-2p$ orbitals contributed to the conduction band at higher energies, while the contribution of $O-2p$ orbitals was minor and can be neglected. The PDOS for each element that contributed to the electronic band structure of the BNT(110) surface revealed a significant contribution from $O-2p$ orbitals to the valence band and Bi- 6p and Ti-3d orbitals to the conduction band. Therefore, we suggested that the electrons primarily transition from $O-2p$ orbitals to Ti-3d orbitals and/or Bi- 6p orbitals. In other words, strong hybridization occurred between $Bi-6p$, Ti- 3d, and $O-2p$ orbitals in the valence band, while the conduction band was composed of Ti-3d orbitals, along with Bi- 6p orbitals and a separated sub-level of Ti-4s orbitals. Our calculation results were consistent with similar features previously predicted for the electronic band structure of bulk and surface BNT materials with rhombohedral symmetry [15, 23, 25, 26].

Figure 3 displays the contribution of the partial spin density of state (PSDOS) of each element and the total spin density of state (TSDOS) for the perfect BNT(110) surface. The upper and lower parts of the horizontal axis were denoted the spin-up and spin-down states of each element's contribution, along with the total spin density of states for the perfect BNT(110) surface. The predictions from PSDOS results align with the calculations presented in Fig. 2(b), demonstrating symmetrical contributions from each element, resulting in the symmetry observed in TSDOS of the BNT(110) surface. Notably, at the E_F, the total spin-up and spindown contributions are equal, indicating that the perfect BNT(110) surface is non-magnetic. Our calculations for the TSDOS of

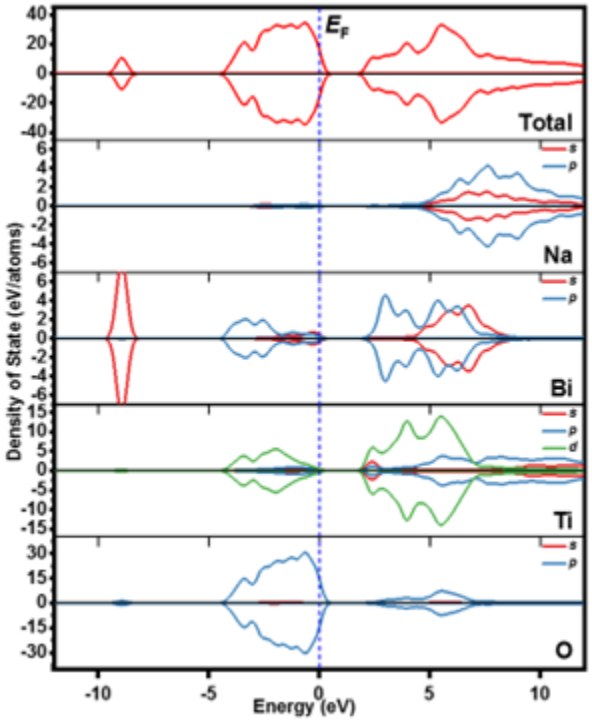

Fig. 3. Partial spin density of state (PSDOS) and total spin density of state (SDOS) of the perfect BNT(110) surface. The E_F is set to zero energy.

the perfect BNT(110) surface are consistent with previous calculations for the BNT(100) surface, which also exhibited non-magnetic behavior [12, 13, 15]. Furthermore, our results for the TS-DOS of the perfect BNT(110) surface align with calculations for bulk BNT materials, confirming that the perfect BNT crystal does not exhibit magnetic properties [25–30]. In other words, both the perfect bulk BNT and the perfect BNT surfaces are non-magnetic, indicating the absence of ferromagnetic behavior in these materials.

Experimental observations have indicated weak ferromagnetism in non-doped BNT materials at room temperature [8,9,12]. However, calculations suggest that the perfect BNT material does not exhibit ferromagnetism. This suggests that the observed weak ferromagnetism in experiments may indeed originate from defects in BNT materials. To investigate this further, we performed detailed calculations for various types of BNT(110) surface defects, including Na, Bi, Ti, and O defect systems.

First of all, we will begin with the Na defect systems, that is, Na vacancy (Na), Na interstitial $(\mathrm{Na_I})$, Na anti-site at Bi-site $(\mathrm{Na_{Bi}})$, and Na anti-site at Ti-site $(\mathrm{Na_{Ti}})$. The influence of each type of defect on the electronic structure of the BNT(110) surface is shown in Figs. 4 (a)-(d) for Nav, Na, $\mathrm{Na_B}$, and $\mathrm{Na_{Ti}}$, respectively. The majority (red bands) and minority (blue bands) states represent the spin-up and spin-down states, respectively. Remarkably, in all four cases of Na defects within the structure, the spin-up and spin-down states are separated, indicating the presence of magnetic moments in the electronic structure. Furthermore, the E_F in the Na, $\mathrm{NaBi_B}$, and Na_{Ti}

defects is located at the top of the valence band, whereas in the Na_I defect, it is positioned closer to the bottom of the conduction band. This suggests that Na_I is *n*-type semiconductor, while Na, Na_{Bi}, and Na_{Ti} are *p*-type semiconductors. The rationale behind this observation is that in a crystal with interstitial Na defects, there is typically an excess of electrons available for conduction, favoring a transition from the *p*-type to the *n*-type semiconductor behavior. Additionally, it is evident that these energy band structures still maintain a well-defined bandgap. However, there are sub-level energy states within the bandgap region, as shown in Fig. 4. These additional sub-level bands contribute to the reduction in the energy gap, leading to increased conductivity characteristics in the presence of defects.

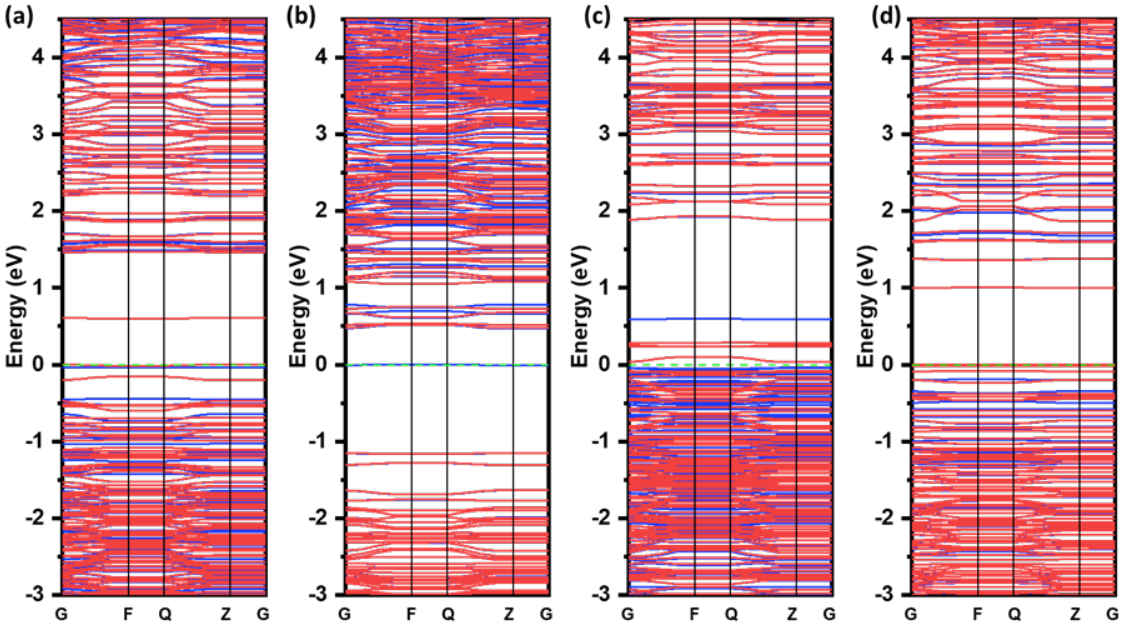

Fig. 4. Electronic band structures of BNT(110) surface with (a) Na vacancy, (b) Na interstitial, (c) Na anti-site at Bi-site defect, and (d) Na anti-site at Ti-site defect. The green dashed lines represent the E_F.

We continue to investigate the magnetic properties of the Na defect system using the SDOS, as shown in Figs. 5(a)-(d) for Na_V, Na_I, Na_{Bi}, and Na_{Ti} defects, respectively. The SDOS displays asymmetry, indicating that the Na defects exhibit magnetism. Based on the SDOS, the observation results of magnetic moment were estimated around $0.52, 0.50, 0.55$, and $0.54\ \mu_B/$ f.u for Na, Na_I, Na_{Bi}, and Na_T, respectively.

In the subsequent investigation, we explored defect systems involving Bi on the BNT(110) surface, including Bi vacancy (Bi_V), Bi interstitial (Bi_I), Bi anti-site at Na-site (Bi_{Na}), and Bi anti-site at Ti-site (Bi_{Ti}). The electronic band structures of Bi_V, Bi_I, Bi_{Na}, and Bi_{Ti} defects are presented in Figs. 6(a)-(d), respectively. Similar to the case of Na defects, Bi defects also exert a significant influence on the energy band structure. Notably, they exhibit behavior as *n*-type semiconductors when the E_F shifts towards the CB bottom, as observed in the cases of Bi_I and Bi_{Na} defects, as

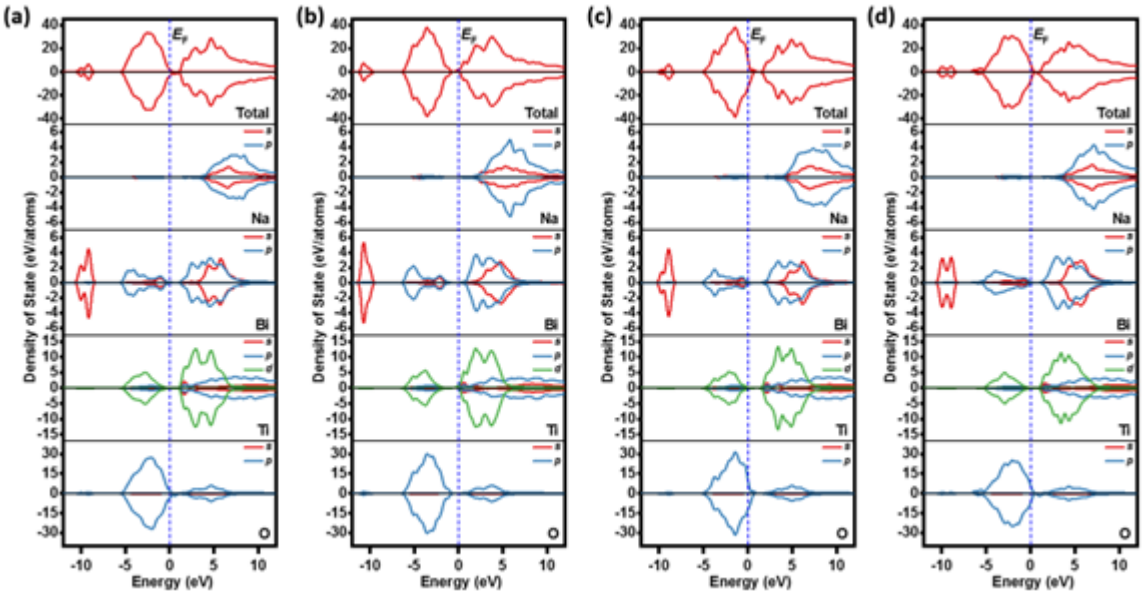

Fig. 5. PSDOS and SDOS of BNT(110) surface with (a) Na vacancy, (b) Na interstitial, (c) Na anti-site at Bi-site defect, and (d) Na anti-site at Ti-site defect.

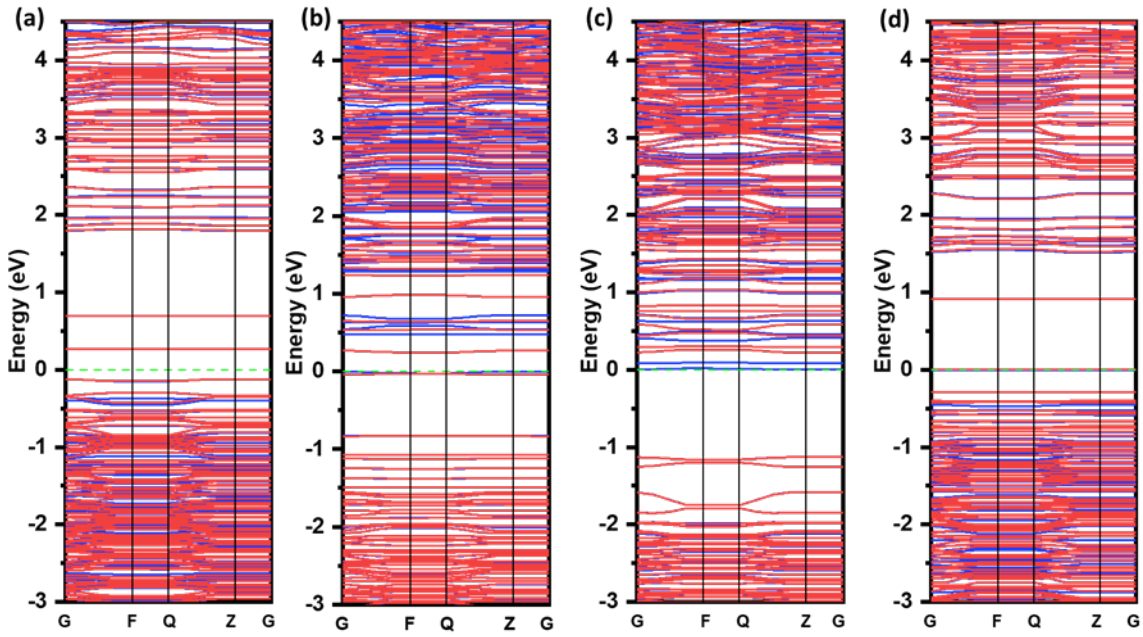

Fig. 6. Electronic band structures of BNT(110) surface with (a) Bi vacancy, (b) Bi interstitial, (c) Bi anti-site at Na-site defect, and (d) Bi anti-site at Ti-site defect. The green dashed lines represent the E_F.

shown in Fig. 6(b) and Fig. 6(c), respectively. Conversely, Biv_V and Bi_{Ti} defects behave as p-type semiconductors, accompanied by the presence of sub-level bands within the bandgap, as shown in Fig. 6(a) and Fig. 6 (d), respectively. This facilitates electron transitions from the VB to the CB. Moreover, in the case of the Biv defect, two additional sub-level bandgaps appear due to the presence of sub-level bands within the bandgap which were presented in the electronic structure of BNT with various Bi-type defects. These sub-level bands are contributed by the oxygen atoms, as will be discussed in the SDOS section below.

Table 1. Magnetization per formula unit cell (μ_B/ f.u.) of BNT (110) surface with various

Defects	$\mathbf{M_{Na}}$ ($\mu_\mathbf{B}$/ f.u.)	$\mathbf{M\ B\ i_{Bi}}$ ($\mu_\mathbf{B}$/ f.u.)	$\mathbf{M_{Ti}}$ ($\mu_\mathbf{B}$/ f.u.)	Mo ($\mu_\mathbf{B}$/ f.u.)	M_{Total} (μ_B/ f.u.)
Pristine	0	0	0	0	0
$\mathbf{Na_V}$	0.01	0.00	0.01	0.50	0.52
$\mathbf{Na_I}$	0.01	0.00	0.47	0.02	0.50
$\mathbf{Na_{Bi}}$	0.03	0.02	0.01	0.01	0.55
$\mathbf{Na_{Ti}}$	0.02	0.01	0.02	0.49	0.54
$\mathbf{Bi_V}$	0.00	0.02	0.02	0.46	0.50
Bi	0.01	0.08	0.39	0.01	0.49
$\mathbf{Bi_{Na}}$	0.00	0.17	0.18	0.04	0.39
$\mathbf{Bi_{Ti}}$	0.00	0.00	0.01	0.49	0.50
$\mathbf{Ti_V}$	0.00	0.00	0.00	0.01	0.01
$\mathbf{Ti_I}$	0.00	0.01	0.01	0.01	0.03
$\mathbf{Ti_{Na}}$	0.02	0.02	0.48	0.01	0.53
$\mathbf{Ti_{Bi}}$	0.01	0.02	0.51	0.03	0.57
$\mathbf{Ov_v}$	0.00	0.00	0.00	0.00	0.00
$\mathbf{O_I}$	0.01	0.01	0.01	0.01	0.04

Figures 7(a)-(d) show the SDOS of Biv_V, Bi_I, Bi_{Na}, and Bi_{Ti} defects, respectively. The observed asymmetry in SDOS indicates the magnetism behavior of Bi defects. Specifically, Biv, Bi, Bi_{Na}, and Bi_{Ti} induce significant magnetic moments of $0.50, 0.49, 0.39$, and $0.50\mu_B$/f.u, respectively (Table 1). The asymmetry in the SDOS primarily originates from the contributions of the O and Ti atoms. This asymmetry is uniformly distributed throughout the energy band structures and is more pronounced in the vicinity of the E_F. Furthermore, this asymmetry is particularly prominent in the SDOS of Ti-3 d and $O-2p$, representing the outermost electron layers of these elements. This observation indicates a rearrangement of positions and the charge correlation exchange within each atom participating in the Ti-O bonding interaction within the defect structure. In the energy band structure of the Biv and Bi Bi_{Ti} defects in Fig. 7(a) and Fig. 7 (d), respectively, the sub-level bands primarily arise from O in the case of Biv, whereas in the case of Bi_{Ti}, they originate from the contribution of Bi. This suggests that the $Bi-O$ ion bonding also plays a crucial role in influencing the electronic structures of the materials.

In this section, we investigated the impact of Ti defects on the electronic structure and magnetic properties of the BNT (110) surface. The defects considered were Ti vacancies (Tiv), Ti interstitials (Ti_I), Ti anti-sites at the Bi-site (Ti_{Bi}), and Ti anti-sites at the Na-site (Ti_{Na})

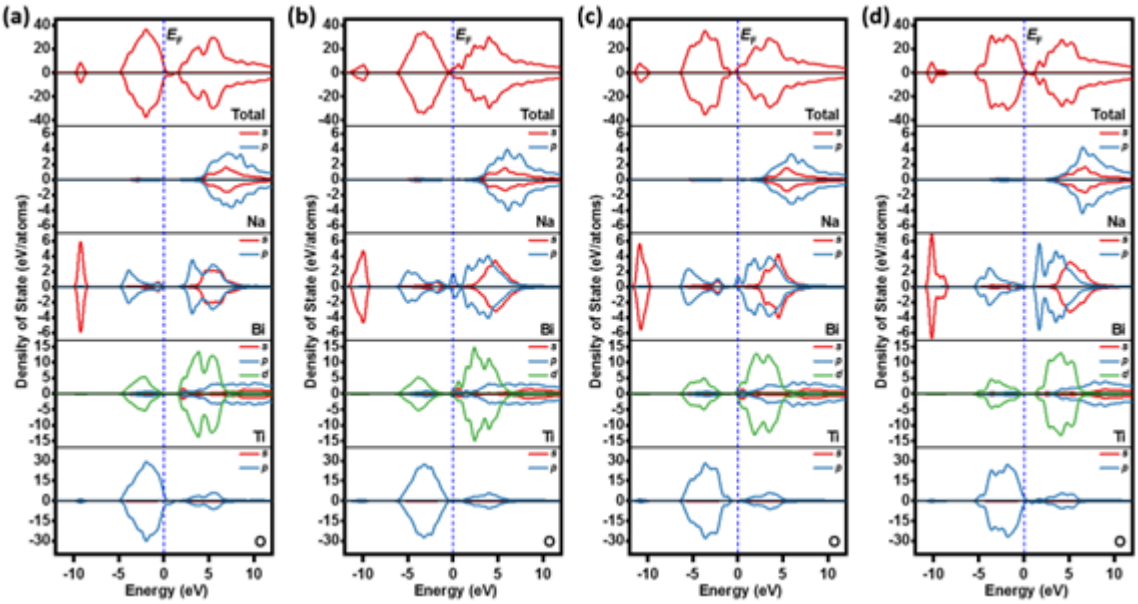

Fig. 7. PSDOS and SDOS of BNT(110) surface with (a) Bi vacancy, (b) Bi interstitial, (c) Bi anti-site at Na-site defect, and (d) Bi anti-site at Ti-site defect.

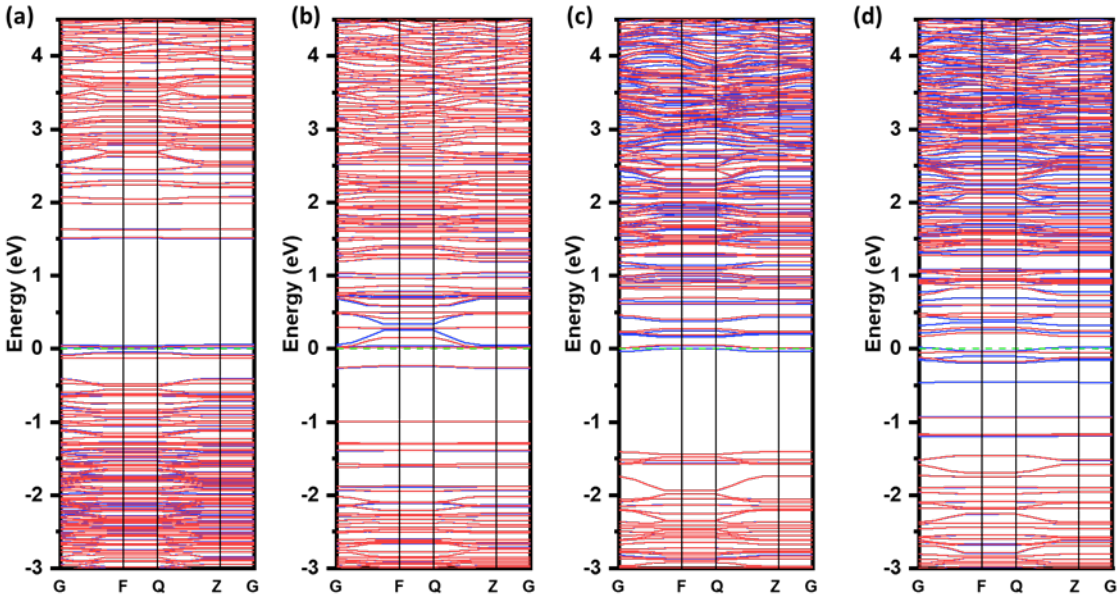

Fig. 8. Electronic band structures of BNT(110) surface with (a) Ti vacancy, (b) Ti interstitial, (c) Ti anti-site at Bi-site, and (d) Ti anti-site at Na-site. The green dashed lines represent the E_F.

The energy band structures for the Ti defects are presented in Figs. 8(a)-(d) for Tiv, Ti I_I, Ti_{Bi}, and Ti_{Na}, respectively. In the case of the Tiv defect, as shown in Fig. 8(a), the material exhibits *p*-type semiconductor behavior. However, Ti_I, Ti_{Bi}, and Ti_{Na} defects behave as *n*-type semiconductors, with the E_F shifted towards the CB of the electronic structure, as shown in Figs. 8(b)-(d), respectively. Additionally, sub-level bands appear in the energy band structure in the case of the Ti_I defect and even more are observed in the Ti_{Na} defect. These sub-level bands narrow the gap between the VB and the CB, indicating higher conductivity. Furthermore, we observe that the energy band structures of the BNT(110) surface with Tiv vacancies appear less dense compared to the energy band structures of the surface with Ti_I interstitial and Ti antisite defects. This discrepancy arises from the fact that Ti has a higher valence electron count compared to Na and Bi. When Ti is in the interstitial position or replaces Na and Bi to form anti-site defects, the valence electron count increases, resulting in a seemingly denser band structure.

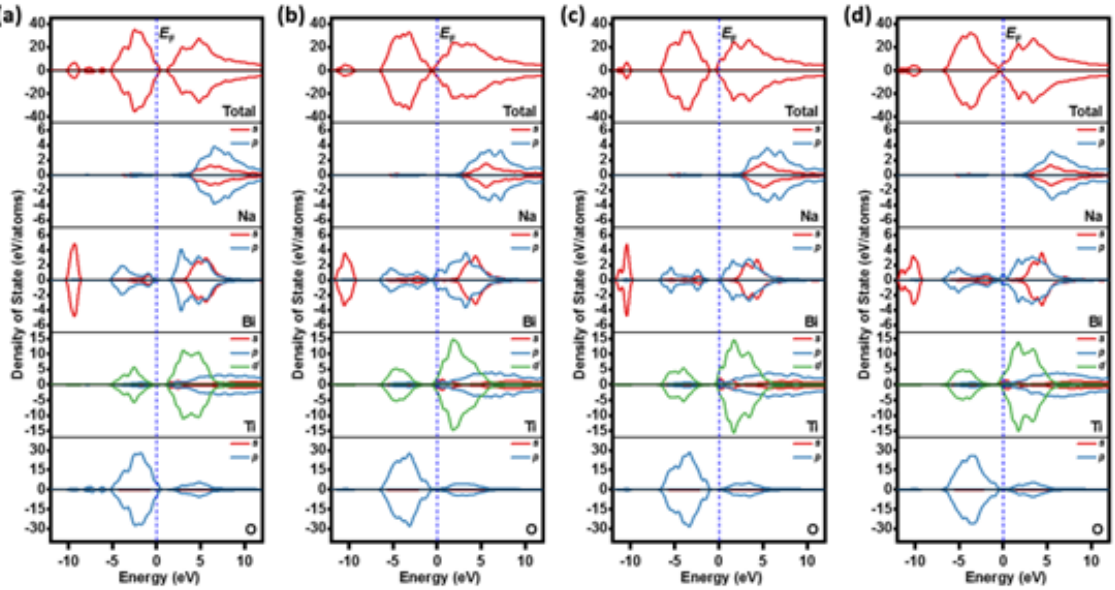

Fig. 9. PSDOS and SDOS of BNT(110) surface with (a) Ti vacancy, (b) Ti interstitial, (c) Ti anti-site at Bi-site defect, and (d) Ti anti-site at Na-site defect.

The SDOS of Tiv, Ti_I, Ti_{Bi}, and Ti_{Na} defects are presented in Figs. 9 (a)-(d), respectively. Observing these results, we can discern various characteristics arising from the defect-induced states in Ti-defect surfaces. In the case of Tiv and Ti_I defects, the SDOS shows almost negligible asymmetry, suggesting a weak presence of defect-induced magnetism (as shown in Figs. 9 (a,b)). These SDOS results are consistent with the magnetic moment values from the elemental contributions, as shown in Table 1, where the total magnetic moment from Tiv and Ti_I defects is only $0.01\mu_B$/ f.u and $0.03\mu_B$/ f.u, respectively. In the cases of Ti_{Bi} and Ti_{Na} defects (Figs. 9 (c,d)), the total magnetic moment values are significantly higher, with values of $0.57\mu_B$/ f.u and $0.53\mu_B$/ f.u, respectively. Accordingly, asymmetry is observed in the SDOS of Ti_{Bi} and Ti_{Na} defects. This observed asymmetry mainly originates from the Ti-3d states. Additionally, when comparing the

SDOS of Bi, differences are evident in the SDOS of the s orbital states around -10eV. Specifically, in the Tiv defect, only one peak is observed, while in the Ti_{Bi} defect, there is a high-intensity peak with a small peak appearing nearby. Similarly, in the Ti_{Na} defect, there is also a small peak at this position. These observations indicate that the electronic components of the Bi-O ionic bonding in these defective crystals are separated into discrete energy levels.

In this section, we will discuss the defect systems related to O on the BNT(110) surface, with a specific focus on two types of defects which were included of O vacancy (O_v) and O interstitial (O_I). Figs. 10(a) and (b) depict the energy band structures of O_V and O_I, respectively. In both cases, the presence of sub-level bands within the bandgap region results in a reduction of the gap between the valence and conduction bands. These sub-level bands align specifically with the E_F, indicating that they are occupied by electrons. This occupancy significantly enhances conductivity by providing ample energy states for electron movement. Consequently, the electronic and thermal properties of the material, including its electrical and thermal conductivity, are influenced by the presence of these sub-level bands at the E_F. It is noteworthy that the E_F in O_V and O_I is not close to the top of the VB or the bottom of the CB, indicating that these structures are intrinsic semiconductors.

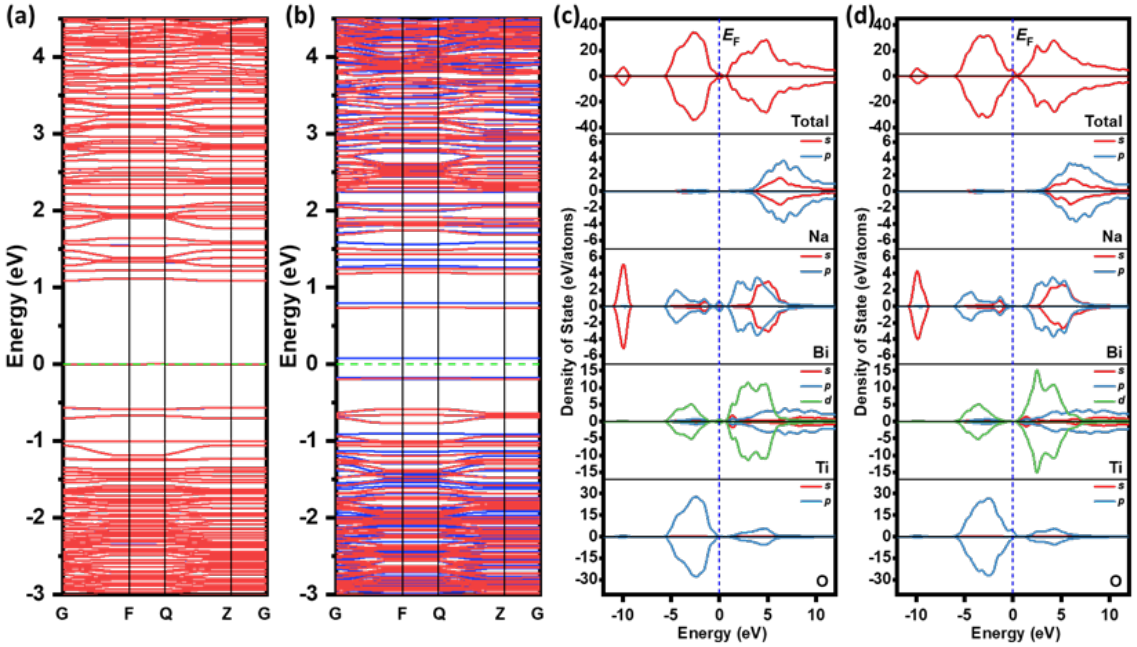

Fig. 10. Electronic band structures and SDOS of $BNT(110)$ surface with $(a,c)O$ vacancy and (b,d) O interstitial defect, respectively. The green dashed lines represent the E_F.

The magnetic properties of the O defects on the BNT(110) surface were examined through the SDOS results (Fig. 10(c), (d)) and the magnetic moment values (Table 1). It was observed that O_V defects did not exhibit any magnetic properties, while O_I defects displayed a slight magnetic moment of $0.04\mu_B/$ f.u. The magnetic contribution in the case of O_I defects originated from the electronic orbital states of $O(O-2p)$. In particular, the SDOS revealed that the sub-level bands

at the E_F in the O_V defect were attributed to the valence electronic orbital states of $Bi(Bi-6s)$, whereas for O_I defects, they were contributed by the $O-2p$ orbital states. Overall, these findings suggest that the O_I defects possess a mild magnetic property, while O_V defects do not exhibit any significant magnetic behavior on the BNT(110) surface.

4. Conclussion

In conclusion, our study employing the DFT method investigated defects on the BNT(110) surface. We observed that the BNT(110) surface exhibited non-magnetic behavior, but the introduction of defects resulted in the emergence of complex magnetic moments, dependent on the defect type. The presence of self-defects caused significant modifications to the electronic band structure, leading to the appearance of a localized energy level within the bandgap. Moreover, the characteristics of the $O-2p, Bi-6p$, and Ti-3d partial density of states were notably affected by both the defect type and elemental defects, resulting in alterations in the magnetic and optical properties. These findings hold great promise for controlling the magnetic and optical properties of lead-free ferroelectric materials by manipulating surface defects, thereby opening up new avenues for advanced electronic applications.

Acknowledgment

This research is funded by Vietnam National Foundation for Science and Technology Development (NAFOSTED) under grant number 103.02-2019.366.

References

[1] N. D. Quan, L. H. Bac, D. V. Thiet, V. N. Hung, and D. D. Dung, *Current development in leadfree* $Bi_{0.5}(Na,K)_{0.5}TiO_3$*-based piezoelectric materials*, Adv. Mater. Sci. Eng. **2014** (2014) 365391.

[2] S. Zhang, B. Malic, J. F. Li, and J. Rodel, *Lead-free ferroelectric materials: Prospective applications*, J. Mater. Res. **36** (2021) 985.

[3] G. A. Prinz, *Magnetoelectronics applications*, J. Magn. Magn. Mater. **200** (1999) 57.

[4] M. Kumar, S. Shankar, A. Kumar, A. Anshul, M. Jayasimhadri and O. P. Thakur, *Progress in multiferroic and magnetoelectric materials: applications, opportunities and challenges*, J. Mater. Sci.: Mater. Electron. **31** (2020) 19487.

[5] N. A. Hill, *Why are there so few magnetic ferroelectrics?*, J. Phys. Chem. B **104** (2000) 6694.

[6] N. A. Benedek and C. J. Fennie, *Why are there so few perovskite ferroelectrics?*, J. Phys. Chem. C **117** (2013) 13339.

[7] I. H. Lone, J. Aslam, N. R. E. Radwan, A. H. Bashal, A. F. A. Ajlouni and A. Akhter, *Multiferroic* ABO_3 *transition metal oxides: a rare interaction of ferroelectricity and magnetis*, Nanoscale Res. Lett. **14** (2019) 142.

[8] L. T. H. Thanh, N. B. Doan, N. Q. Dung, L. V. Cuong, L. H. Bac, N. A. Duc, P. Q. Bao, and D. D. Dung, *Origin of room temperature ferromagnetism in Cr-doped lead-free ferroelectric* $Bi_{0.5}Na_{0.5}TiO_3$ *materials*, J. Electron. Mater. **46** (2017) 3367.

[9] D. D. Dung, N. T. Hung and D. Odkhuu, *Structure, optical and magnetic properties of new* $Bi_{0.5}Na_{0.5}TiO_3 - SrMnO_{3-\delta}$ *solid solution materials*, Sci. Rep. **9** (2019) 18186.

[10] D. E. J. Ruth, R. A. U. Rahman, B. Sundarakannan and M. Ramaswamy, *Room temperature multiferroicity and magnetoelectric coupling in Na-deficient sodium bismuth titanate*, Appl. Phys. Lett. **114** (2019) 062902.

[11] R. Pattanayak and S. Panigrahi, *Electric and magnetic transport analysis of* $Na_{0.5}Bi_{0.5}TiO_3$ *nanoparticles for temperature and magnetoimpedance sensor applications*, J. Magn. Magn. Mater. **481** (2019) 162.

[12] L. Ju, C. Shi, L. Sun, Y. Zhang, H. Qiu and J. Hu, *Room-temperature magnetoelectric coupling in nanocrystalline* $Na_{0.5}Bi_{0.5}TiO_3$, J. Appl. Phys. **116** (2014) 083909.

[13] L. Ju, T. Xu, Y. Zhang, C. Shi, and L. Sun, *Ferromagnetism of* $Na_{0.5}Bi_{0.5}TiO_3(100)$ *surface with* O_2 *adsoprtion*, Appl. Surf. Sci. **412** (2017) 77.

[14] Y. Zhang, J. Hu, F. Gao, H. Liu and H. Qin, *Ab initio calculation for vacancy-induced magnetism in ferroelectric* $Na_{0.5}Bi_{0.5}TiO_3$, Comp. Theor. Chem. **967** (2011) 284.

[15] V. T. Lam, N. H. Thoan, N. N. Trung, D. Q. Van, and D. D. Dung, *Surface ferromagnetism of complex defects lead-free ferroeletric* $Bi_{0.5}Na_{0.5}TiO_3$ *materials*, Surf. Inter. Ana. **55** (2023) 243.

[16] S. J. Clark, M. D. Segall, C. J. Pickard, P. J. Hasnip, M. J. Probert, K. Refson and M. C. Payne, *First principles methods using CASTEP*, Z. Kristallogr. Cryst. Mater. **220** (2005) 567.

[17] J. P. Perdew, K. Burke, and M. Ernzerhof, *Generalized gradient approximation made simple*, Phys. Rev. Lett. **77** (1996) 3865.

[18] H. J. Monkhorst, and J. D. Pack, *Special points for Brillouin-zone integrations*, Phys. Rev. B **13** (1976) 5188.

[19] H. Lü, S. Wang, and X. Wang, *The electronic properties and lattice dynamics of (* $Na_{0.5}Bi_{0.5}$*)*TiO_3 *: From cubic to tetragonal and rhombohedral phases*, J. Appl. Phys. **115** (2014) 124107.

[20] G. O. Jones and P. A. Thomas, *Investigation of the structure and phase transitions in the novel A site substituted distorted perovskite compound* $Na_{0.5}Bi_{0.5}TiO_3$, Acta Crystallogr. B **58** (2002) 168.

[21] E. Mosconi, A. Amat, M. K. Nazeeruddin, M. Gratzel, and F. D. Angelis, *First-Principles modeling of mixed halide organometal perovskites for photovoltaic applications*, J. Phys. Chem. C **117** (2013) 13902.

[22] J. Padilla, and D. Vanderbilt, Ab initio study of $BaTiO_3$ surfaces, Phys. Rev. B **56** (1997) 1625.

[23] S. Behara, G. S. Priyanga, and T. Thomas, *Strain-induced effects in the electronic and optical properties of* $Na_{0.5}Bi_{0.5}TiO_3$ *: An ab-initio study*, Mater. Today Comm. **24** (2020) 101348.

[24] C. He, Y. Zhang, L. Sun, J. Wang, T. Wu, F. Xu, C. Du, K. Zhu, and Y. Liu, *Electrical and optical properties of* Nd^{3+}*-doped* $Na_{0.5}Bi_{0.5}TiO_3$ *ferroelectric single crystal*, J. Phys. D: Appl. Phys. **46** (2013) 245104.

[25] D. D. Dung, N. H. Thoan, N. Q. Dung, N. H. Lam, P. V. Vinh, V. T. Lam, P. D. Luong, and D. Q. Van, *Structural, optical, and magnetic properties of a new complex (1-x)* $Bi_{1/2}Na_{1/2}TiO_3 + xMgNiO_{3-\delta}$ *solid solution system*, Appl. Phys. A **128** (2022) 129.

[26] D. D. Dung, N. H. Thoan, P. V. Vinh, N. H. Lam, V. T. Lam, P. D. Luong, D. Q. Van, and D. Odkhuu, *Magnetic properties of new* $(1-x)Bi_{1/2}Na_{1/2}TiO_3 + xBaNiO_{3-\delta}$ *solid solution materials*, Appl. Phys. **A 128** (2022) 168.

[27] N. T. Hung, N. H. Lam, A. D. Nguyen, L. H. Bac, N. N. Trung, D. D. Dung, Y. S. Kim, N. Tsogbadrakh, T. Ochirkhuyag, and D. Odkhuu, *Intrinsic and tunable ferromagnetism in* $Bi_{0.5}Na_{0.5}TiO_3$ *through* $CaFeO_{3-\delta}$ *modification*, Sci. Rep. **10** (2020) 6189.

[28] D. D. Dung, N. H. Lam, A. D. Nguyen, N. N. Trung, N. V. Duc, N. T. Hung, Y. S. Kim, and D. Odkhuu, *Experimental and theoretical studies on induced ferromagnetism of new (1x)* $Na_{0.5}Bi_{0.5}TiO_3 + xBaFeO_{3-\delta}$ *solid solution*, Sci. Rep. **11** (2021) 8908.

[29] D. D. Dung, N. H. Thoan, N. Q. Dung, P. V. Vinh, N. H. Lam, V. T. Lam, P. D. Luong, and D. Q. Van, Magnetic properties of a (1-x) Bi.5 $Na_{0.5}TiO_3 + xCaNiO_{3-\delta}$ solid solution system prepared by sol-gel technique, J. Electron. Mater. **51** (2022) 1905.

[30] D. D. Dung, N. H. Thoan, N. Q. Dung, H. H. Lam, V. T. Lam, P. V. Vinh, P. D. Luong, and D. Q. Van, *Synthesis and characterization of (1-x)* $Bi_{1/2}Na_{1/2}TiO_3 + xSrNiO_{3-\delta}$ *solid solution system*, J. Electron. Mater. **51** (2022) 2716.